J Nondestruct Eval (2014) 33:711–723
DOI 10.1007/s10921-014-0265-5

Relation of Electromagnetic Emission and Crack Dynamics in Epoxy Resin Materials

S. O. Gade · U. Weiss · M. A. Peter · M. G. R. Sause

Received: 30 May 2014 / Accepted: 23 September 2014 / Published online: 7 October 2014

Abstract Electromagnetic emission (EME) testing and acoustic emission (AE) testing are applied to investigate the failure of a brittle, dielectric material under mechanical load. A setup for three point flexure tests comprising simultaneous monitoring of EME and AE was used to induce fracture of epoxy resin specimens. The influences of the orientation and the distance of the crack surface on the detectable EME signals are the subjects of investigation. As EME sensor a capacitive sensor was used. Tests with an artificial test source are carried out to characterize the system response of the sensor, the attached amplifier and acquisition cards as well as the included bandpass filters. We propose an EME source based on the surface charge density modelled at the position of the fracture plane. Results of finite element method modelling of the EME source are compared to experimental results and show very good agreement. The experimental results show a clear directional character of the emitted electromagnetic field and a strong dependence of the detected signals amplitude on source-sensor distance. A significant influence of the measurement chain on the detected electromagnetic signals bandwidth was found. Furthermore it is shown that the electromagnetic signals consist of three contributions originating from different source mechanisms. These are attributed to the separation and relaxation of charges during crack growth and to the vibration of the charged crack surfaces.

Keywords Electromagnetic emission · Acoustic emission · Fracture · Epoxy resin · Transfer function · Finite element modelling

S. O. Gade (✉) · M. G. R. Sause
Institute for Physics, University of Augsburg, Experimentalphysik II, Universitätsstrasse 1, 86159 Augsburg, Germany
e-mail: sebastian.gade@physik.uni-augsburg.de

U. Weiss · M. A. Peter
Institute of Mathematics, University of Augsburg, Universitätsstrasse 14, 86159 Augsburg, Germany

M. A. Peter
Augsburg Centre for Innovative Technologies, University of Augsburg, 86135 Augsburg, Germany

1 Introduction

The emission of electromagnetic fields during failure of different materials is a phenomenon which has been under investigation for many decades. The occurrence of this electromagnetic emission (EME) has been shown for almost any material and for various kinds of failure mechanisms [1–9]. The detection and analysis of EME can help to understand the complex processes of crack formation. This is especially useful when accompanied by other, nondestructive testing (NDT) methods like the examination of crack induced acoustic emission (AE). Many theories about the sources of EME exist. The origins of these emitted fields differ for different materials and failure modes. Even for materials which have been under investigation for decades, the sources of EME are still discussed controversially. A comprehensive review on the lack of consistency of current models and their discrepancy with recent experiments is given by Frid et al. [2]. Some authors attribute the dynamics to the mechanical vibration of the crack surface [1,3]. In contrast, Frid et al. and Rabinovitch et al. suggest to describe EME in the form of charge surface vibrational waves [2,4,10]. Also there are still inconsistencies of the proposed models and experimental results, e.g. regarding the occurrence of EME under shear crack propagation [2,4,11–13]. Furthermore, other sources such as inertial and quadrupole polarizations of a dielectric are discussed as well [14].

Detecting EME during fracture of materials offers the possibility to monitor the process of crack initiation and crack propagation. According to [8] the detectable signals are a function of the orientation of the crack surfaces relative to the sensor. Furthermore, the signals may contain information about the spatial and temporal characteristics of their sources [2].

There are different measurement techniques established to detect EME which can be categorized into electric dipole sensors and magnetic dipole sensors [15]. The latter group is applied to measure magnetic fields and comprises inductive sensors such as loops and coils. These may exhibit strong resonances in the frequency region of interest, although attempts were made to improve the frequency characteristics of inductive sensors [16]. Capacitive sensors such as capacitors or antennas are used to measure electric fields. These sensors provide relatively flat characteristics over a wide range of frequencies [17]. A theoretical review of capacitive probes is given by Partridge in [18]. Capacitive probes can be used as electric potential sensors to measure electric fields with no significant perturbation to the field [19]. Capacitive sensors with an attached measurement circuit are a common tool to measure the electromagnetic field generated by fracture of materials [20].

In brittle materials fracture occurs with little or no plastic deformation. The crack propagation is unstable and typically causes brittle failure. For mode I fracture the dominant x-displacement of the crack surfaces develops perpendicular to the yz-plane of the crack (Fig. 1). When the crack propagates along the z-axis molecular bonds are breaking and charges appear at the crack surface. This leads to an asymmetric charge separation for a reason that is still not fully understood [12]. It has to be noted that this break of symmetry is questioned by some authors [2,4,21]. However, similar

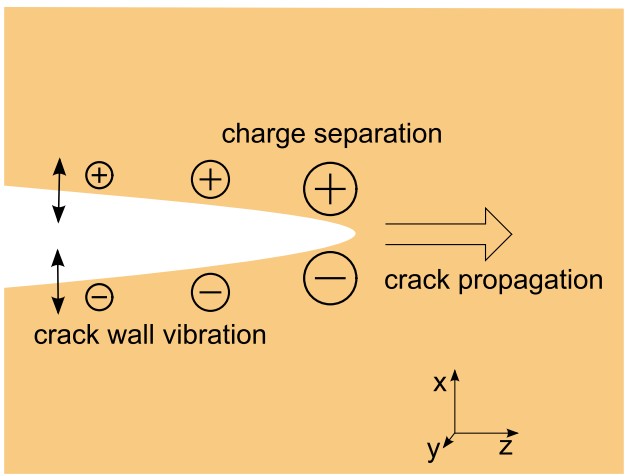

Fig. 1 Basic model of a mode I based crack propagation with a charge imbalance. Remaining charges at the crack surfaces are moving according to the crack wall vibrations

effects are known for other dielectric solids [22]. The temporal characteristic of the resulting charge distribution is related to the propagation velocity of the crack tip. Hence, a constant crack velocity would result in a linearly rising charge density. The separated charges then recombine with a relaxation time constant depending on the dielectric properties of the material and on the geometry of the crack. The combination of both effects causes a temporal increase of charges due the process of crack propagation and a subsequent decrease due to charge relaxation. In addition to the generation of charges at the crack tip, the charges present at the crack surfaces will move together with the crack surface as long as they are present.

The formation of cracks and the vibration of the generated crack walls is accompanied by the generation of acoustic waves. This phenomenon is generally referred to as AE. The frequencies of the acoustic waves typically are in the ultrasonic range. The detection and the analysis of the AE signals are a commonly used practice for the investigation of failure in solid materials. Piezoelectric sensors are able to detect amplitudes down to $2.5 \cdot 10^{-14}$ m [23] and special broadband sensors offer a relatively flat frequency response in the frequency region of interest [24].

Numerical simulations have proved to be a powerful tool for the calculation of complex physical systems or problems which cannot be solved analytically. By using the appropriate physical equations and by paying attention to the physical content of the simulation, the solution can contribute to a better understanding of the modelled phenomenon. The finite element method (FEM) is a numerical technique which has been shown to be applicable for many physical problems. With this approach it is possible to model e.g. crack growth [25,26], AE sources [27], the propagation of acoustic waves in isotropic and anisotropic materials [28,29] or even AE sensor signals [30].

FEM modelling also has been used for decades to solve various electrodynamic problems [31,32]. But, to the best of the author's knowledge, to this date no numerical simulations about EME generated by fracture were performed.

In this paper a method to analyze the EME signals from fracture in brittle dielectrics is introduced. Experiments with a test source were performed to study the influence of the applied capacitive sensor system and measurement chain on different test signals. An experimental setup was developed to induce fracture to epoxy resin specimens and to detect the occurring electromagnetic and AE signals. The cracks exhibit a defined orientation and provide a reproducible source of EME signals. Therefore, the influence of the source-sensor distance and the angle of orientation between crack surface and capacitive sensor plate can be analyzed. The recorded EME waveforms are compared to the respective AE signals. Moreover, FEM simulations were carried out to study basic characteristics of the emitting source and to quantify

the influences of the measurement system on the detected signal. The modelling includes a three-dimensional representation of the experimental situation including the model source, the EME sensor and the characteristics of the measurement electronics. The influence of the electrical circuit is taken into account by a transfer function derived from experimental data.

2 Experimental

2.1 Experimental Setup

In order to characterize our measurement system, we first carried out investigations using an artificial test source. This test source consists of a small antenna of 5 mm length which is coupled to an Agilent 33210A arbitrary waveform generator. The small dimensions of the antenna result in a resonance frequency in the GHz range. Therefore, the radiated power was considered constant for frequencies below 1 MHz. Specific waveforms which resemble the hypothetical temporal characteristics of the electric field as a function of crack growth were generated and emitted by the antenna. Antenna and sensor are positioned next to each other with a distance of 1 mm. Thus sensor plate and test source form a capacitor with a frequency dependent capacitive reactance.

To determine the influence of this reactance and to verify the suitability of this kind of test source, periodic voltage signals were generated with the arbitrary waveform generator within a frequency range of 100 Hz–1 MHz and an amplitude of 1 V. The signals were emitted by the antenna and detected by the sensor plate. To eliminate possible influences of the preamplifier circuit the signals are recorded with an oscilloscope (GaGe CompuScope 14200) and without any preamplification. The sampling rates were varied between 0.1 and 200 MS/s depending on the input frequencies. The signal strength of the detected signals in relation to the input signal strength and an equivalent circuit of the setup are shown in Fig. 2. The measured voltages are in the range of 3–7 mV since no preamplifier was used. Between 500 Hz and 1 MHz no resonances were found. Frequencies below 500 Hz suffer from a reduction in detected signal amplitude because the circuit forms a high pass filter. A calculation for the equivalent circuit with $R_{BNC} = 10\,\Omega$, $R_{OSC} = 1\,M\Omega$, $C_{BNC} = 84\,pF$, $C_{OSC} = 40\,pF$ and a measured capacitance of the antenna-sensor system of $C_{A-S} \approx 1$ pF results in a high pass characteristic with a cut-off frequency of about 1 kHZ.

The equivalent circuit for measuring the EME signals of the specimen is similar to the one shown in Fig. 2. The capacitance of the antenna-sensor system has to be replaced with the capacitance of the sensor alone which was calculated to be $C_S \approx 0.5$ pF and the load impedance and resistance of the oscilloscope have to be replaced with the corresponding values of the preamplifier. The input voltage then represents the voltage at the sensor plate. The capacitance of the antenna-sensor system and the sensor plate are of the same order of magnitude and small when compared to the other capacitances of the circuit. Therefore, the influence of the antenna on the transfer function in Fig. 2 and on the transfer function of the measurement chain used later is considered minimal.

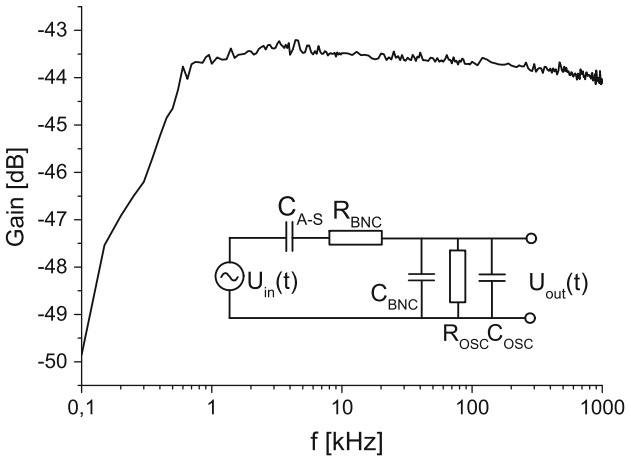

Fig. 2 Frequency response of the antenna-sensor system

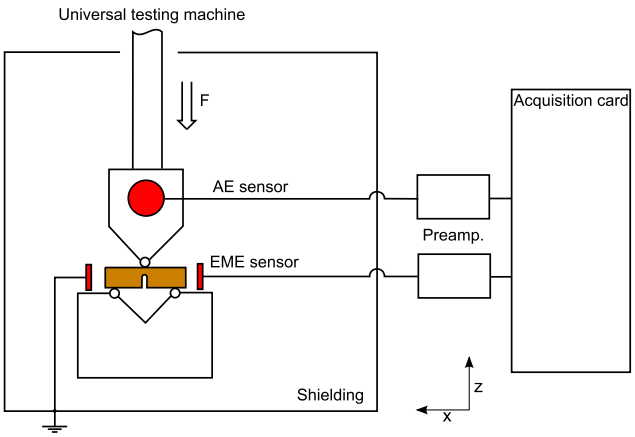

Fig. 3 Diagram of experimental set-up consisting of universal testing machine, test fixture, electromagnetic shielding and EME and AE sensors with measurement equipment

An experimental setup to investigate electromagnetic and acoustic emission generated by fracture of polymer specimens was developed (Fig. 3). To induce the fracture of single edge notched bend specimens, three point bending tests were performed.

Identical specimens with dimensions shown in Fig. 4 were prepared. Partially cured RTM6 epoxy resin plates of 5 mm thickness were prepared. For this purpose, casting molds made from two component silicon rubber (Elastosil M 4601 A/B) were filled with the viscous resin and then heated for the curing process. For 80 % cross-linked resin plates this process uses curing at 120 °C for 30 min followed by a post-

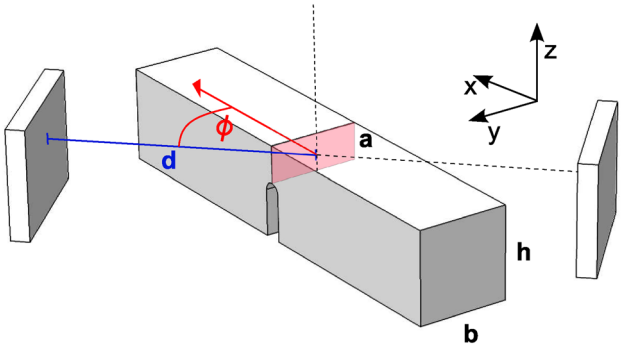

Fig. 4 Schematic diagram of the electromagnetic sensor plates arrangement and RTM6 specimen with parameters

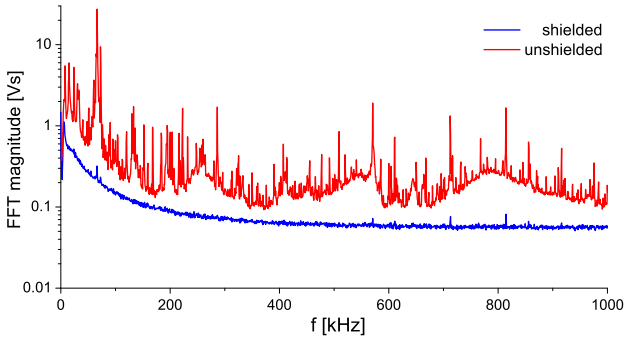

Fig. 5 Frequency spectrum of measured electromagnetic noise with and without shielding

cure at 135 °C for 140 min, with heating and cooling rates of 2 K/min [33]. The degree of cross-linking was determined by using differential scanning calorimetry (DSC) [33]. Then, the plates were cut to beams with lengths of 25 mm and widths of b = 5 mm. Notches of 3 mm length and 1 mm width were added leaving a thickness of a = 2mm at the centre of the specimens.

In order to investigate the relation between measured EME signal strengths and relative position of sensor plates and EME source it is advantageous to create a source with a distinct orientation. The fracture surfaces obtained for our notched RTM6 specimen were found to show only a variance in orientation of $\phi \leq 5°$.

A bend fixture with a support span of 20 mm and a pin radius of 1.5 mm was used. The whole fixture was created from nonconducting materials. The load pins were made of polyvinyl chloride (PVC) and the rest of the fixture was made of polymethyl methacrylate (PMMA). This was necessary since all conductors influence the field distribution and therefore would decrease the sensitivity of the sensor [34]. Therefore, the fixture exhibits a high compliance with regard to the specimens. This compliance of the fixture alone was measured to be 1.03 µm/N which is 17.5 % of the total compliance during the flexure tests.

A universal testing machine (Zwick ZT 5.0) was used to apply a mechanical load with a constant velocity of 5 mm/min. The load was measured with a 5 kN Xforce HP load cell.

For the detection of the acoustic signals a KRN type "Glaser" sensor with flat frequency response was attached to the fixture above the loading pin (see Fig. 3). The AE signal was preamplified by 20 dB using a type 2/4/6 preamplifier without internal bandpass filter. A trigger based acquisition was used with a threshold of 35 dB_{AE}. The signals were recorded using a PCI-2 system (Mistras, software: AEWin) with 10 µs Peak-Definition-Time (PDT), 80 µs Hit-Definition-Time (HDT), 300 µs Hit-Lockout-Time (HLT) and a 1 kHz–3 MHz bandpass filter (1 kHz 4th order Butterworth high pass and 3 MHz 6th order Butterworth low pass, with rectangular window function) as software settings.

The electromagnetic signals were detected using two small copper plates of 6 mm height and 8 mm width forming a capacitor. While one of the plates was grounded the other one was connected to a 2/4/6 preamplifier without internal bandpass filter. The signals were amplified by 40 dB and were also acquired with the PCI-2 system. A 35 dB_{AE} threshold, 50 µs PDT, 1,000 µs HDT, 1,000 µs HLT and the same 1 kHz–3 MHz bandpass filter were used for detection.

Finally the whole setup was shielded against electromagnetic noise and electrically insulated from the universal test machine. The shielding consists of a grounded aluminium box of 3 mm thickness. Such boxes have been shown to provide good shielding effects at low frequencies [35]. No significant influences of seam leakage was observed. Holes cut into the box for the load transmission and cables did not reduce the shielding effectiveness since their dimensions are much smaller than the wavelengths of the electromagnetic field for frequencies below 1 MHz. Thus, the holes operate as wave guides below their cutoff frequencies. Figure 5 shows the averaged frequency spectrum of the electromagnetic noise detected with the capacitive sensor with and without an appropriate shielding. With a grounded shielding box applied, the measured electromagnetic noise could be reduced up to one order in magnitude.

For the modelling of the experiment the dielectric properties of RTM6 were measured using a frequency response Novocontrol alpha-analyzer (frequency range from 1 Hz to 10 MHz), an autobalance bridge Agilent 4980A (20 Hz–2 MHz), and an impedance/material analyzer Agilent E4991A (1 MHz–3 GHz).

Modelling

The experimental setup was modelled using the "Electric Currents" module of the software COMSOL Multiphysics, which is based on the finite element method. With this model,

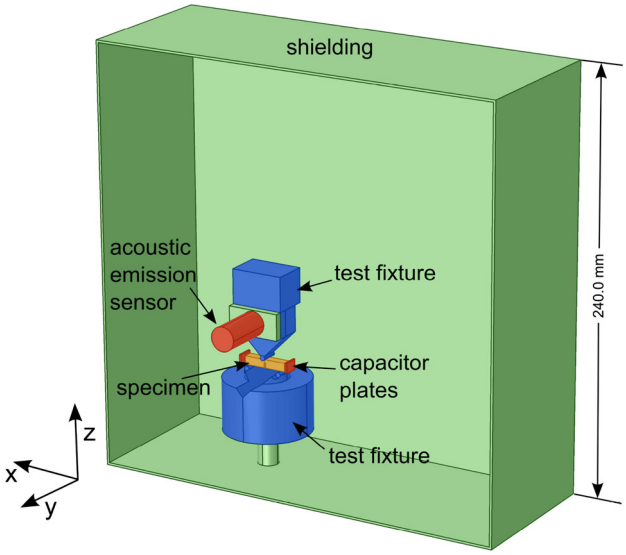

Fig. 6 3D geometry of the simulation model. *Green* grounded metal parts, *blue* nonconducting parts, *red* sensors, *orange* RTM6 specimen (Color figure online)

the electric field respectively the electric potential in the vicinity of the setup can be calculated directly. A quasi-stationary approach was chosen due to the fact that the wavelengths of the occurring electric fields are much larger than the dimensions of the experimental setup, hence the quasi-stationary conditions ($\lambda \gg d$) are satisfied. To enable a comparison of simulated and experimentally obtained electromagnetic signals we use a 3D geometry based on the used experimental setup. Figure 6 shows the model geometry, consisting of the RTM6 specimen (orange), the test fixture made of nonconducting materials (blue), the grounded shielding box and other conducting parts (green) and the EME and AE sensors (red). All boundaries of left capacitor plate, the bolt, the acoustic sensor and the shielding box are grounded in accordance with the experimental setup. Careful geometrical simplifications were made for details of components as screws, sensor holders and the acoustic sensor, which are not expected to considerably influence the calculated electric field.

The corresponding material properties were assigned to the domains that represent the nonconducting parts of the model and to the void space. The dielectric properties of these materials are summarized in Table 1. All conducting parts were modelled by appropriate boundary conditions. Thus, these parts were considered as ideal conductors. Ground boundary conditions were assigned to all grounded parts, i.e. the shielding box, the acoustic sensor and the bolt on which the fixture is mounted on. The sensor plate was modelled with a floating potential boundary.

The fracture of the specimen or any other mechanical movement was not considered in the present model. As source function a time dependent surface charge located

Table 1 Dielectric properties of the materials applied in the model

Material	ϵ_r	σ (S/m)	Sources
PVC	2.9	1e-14	[36,37]
PMMA	3.0	1e-14	[36,38]
RTM6	4.12538	6.668e-10	Measured
Air	1.00059	8e-15	[39,40]

at the hypothetical crack surface and the time dependent generation of the respective electric field is used. The electric potential V is calculated by solving a current conservation problem based on Ohm's law:

$$\nabla \cdot \mathbf{J} = 0, \tag{1}$$

$$\mathbf{J} = \left(\sigma + \epsilon_0 \epsilon_r \frac{\partial}{\partial t}\right) \mathbf{E}, \tag{2}$$

$$\mathbf{E} = -\nabla V, \tag{3}$$

where σ is the electrical conductivity and ϵ_r the relative permittivity of the respective material and ϵ_0 is the electric permittivity of free space. Electrically insulated boundaries are simulated by the no-flux condition $\mathbf{n} \cdot \mathbf{J} = 0$ while at grounded boundaries the electric potential is set to zero. We assume a zero-potential at the initiation of our simulations, i.e. V(t=0)=0. The floating potential boundary condition which is assigned to the surface of the sensor plate is realized by the equation:

$$-\int_S \mathbf{J} \cdot d\mathbf{S} = 0. \tag{4}$$

A boundary current source Q_j is defined on the internal boundary of the specimen resembling the crack surface of the experiment:

$$\mathbf{n} \cdot (\mathbf{J}_1 - \mathbf{J}_2) = Q_j. \tag{5}$$

We use quadratic Lagrange elements for the spatial discretization. Based on convergence studies we choose a resolution of the RTM6 specimen with a maximum mesh element scale of 1mm. For the two small copper plates, which form the capacitor for the detection of the electromagnetic signals, a resolution with maximum mesh element size of 4 mm proved sufficient. This resolution was also used for the fixture and the acoustic sensor. The remaining domains, i.e. the air and the shielded and insulated box, are meshed with a maximum element size of 140 mm and with a maximum element growth rate of 1.5. This ensures an adequate resolution in the area between specimen and detector and reduces the degrees of freedom. The time-dependent calculation is done via a Generalized-α-algorithm with a time step size of $5 \cdot 10^{-7}$s.

The design of the Comsol model includes all components of the experimental setup, except for the signal processing part of the measurement instrumentation. The signal of interest is obtained by averaging the calculated electric potential

over the surface of the sensor plate, which forms one part of the sensing capacitor. Feedback of the attached circuit into the model was considered to be negligible. In order to allow comparison with experimentally obtained signals, the influence of the measurement electronics was included by a transfer function which was derived from the test source experiments:

$$H(\omega) = \frac{\mathcal{F}\{u_{MC}(t)\}}{\mathcal{F}\{u_{WG}(t)\}}. \tag{6}$$

Here, $u_{WG}(t)$ is the input signal generated by the waveform generator, $u_{MC}(t)$ is the resulting signal measured by the sensor system and $\mathcal{F}\{u_i(t)\}$ are the corresponding Fourier transformed signals. Components for frequencies above 100 kHz were cut from the transfer function since they only resemble the electronic noise floor of the system. The influence of the measured sensor characteristic of the EME sensor (Fig. 2) is considered small when compared to the influence of the rest of the measurement chain.

Results and Discussion

Test Source Results

To improve the understanding of the EME acquisition system, we conducted tests using an artificial test sources powered by an arbitrary waveform generator. The basic hypothesis to follow within the first series of tests was that one part of the signal stems from the separation of charges during crack growth and the second part is due to the subsequent charge relaxation. The combination of these two contributions will be referred to as base signal in the following. As a third part of the signal a small oscillation is superimposed. This oscillation is supposed to originate from the vibrations of the charged crack surfaces.

For the charge separation following the crack tip, the generated electrical field emitted would rise during crack growth due to cumulative charge separation, and then decline with a certain time constant. A corresponding theoretical model for the temporal characteristic of the electric field caused by cracking rocks was reported by Ivanov et al. in [41].

A given charge distribution decays over time due to conduction currents. The charge relaxation time τ for a surface charge at the crack surface of a RTM6 specimen depends on the dielectric properties of RTM6 and the adjacent air. For RTM6 we measured $\sigma = 6.67 \cdot 10^{-10}\,\Omega^{-1}\,cm^{-1}$ and $\varepsilon_r = 4.13$. The charge relaxation time τ also depends on the geometry of the charged surface and the surrounding matter. Furthermore, the dielectric properties are a function of the temperature which is much higher at the crack tip than in the surrounding bulk. Therefore, τ is time and location dependent during the crack propagation process but constant afterwards. For an infinite, uniformly charged plane separating two half spaces of different materials the surface charge relaxation time is calculated by $1/\tau = 1/2(1/\tau_1 + 1/\tau_2)$ with $\tau_i = \varepsilon_i/\sigma_i$. In this case the relaxation time for a surface charge between RTM6 and air is calculated to be $\tau \approx 110\,ms$. This estimation only gives the order of magnitude for the actual time constant because the real crack surfaces are not infinite planes. Since the fracture process is much faster than the relaxation of charges the influence of the surface temperature is not considered in this estimation.

To evaluate the system response to source signals with different relaxation times we generated different signals as seen in Fig. 7 top. These test signals resemble a smoothed step function. All test signals exhibit the same rise characteristic but diminish with different time constants, with a smooth transition between these two parts. The signals were generated with a total length of 2 ms. The first signal does not decay ($\tau = \infty$). The other signals decay with $\tau \approx 600$ and $\tau \approx 200\,\mu s$, respectively. Regarding the estimated charge relaxation time of RTM6 the first signal is considered to represent the experimental conditions.

The according signals detected with our EME sensor are shown in Fig. 7 (bottom). Only a fraction of such slowly

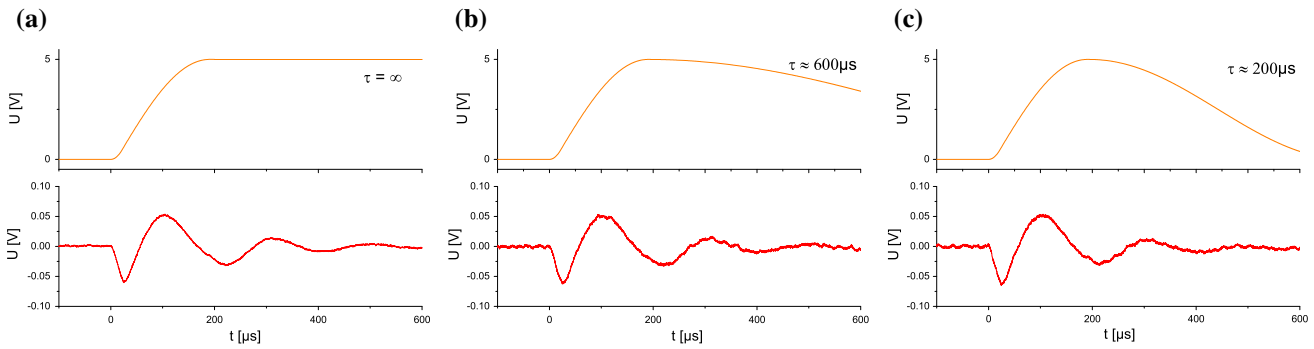

Fig. 7 **a**, **b**, **c** (*Top*) test signals fed to the test source by the arbitrary waveform generator. Each having the same rise characteristic but different decay rates. **a**, **b**, **c** (*Bottom*) the resulting signals measured with the present sensor system. Their *shape* is dominated by the rise characteristic of the test signals

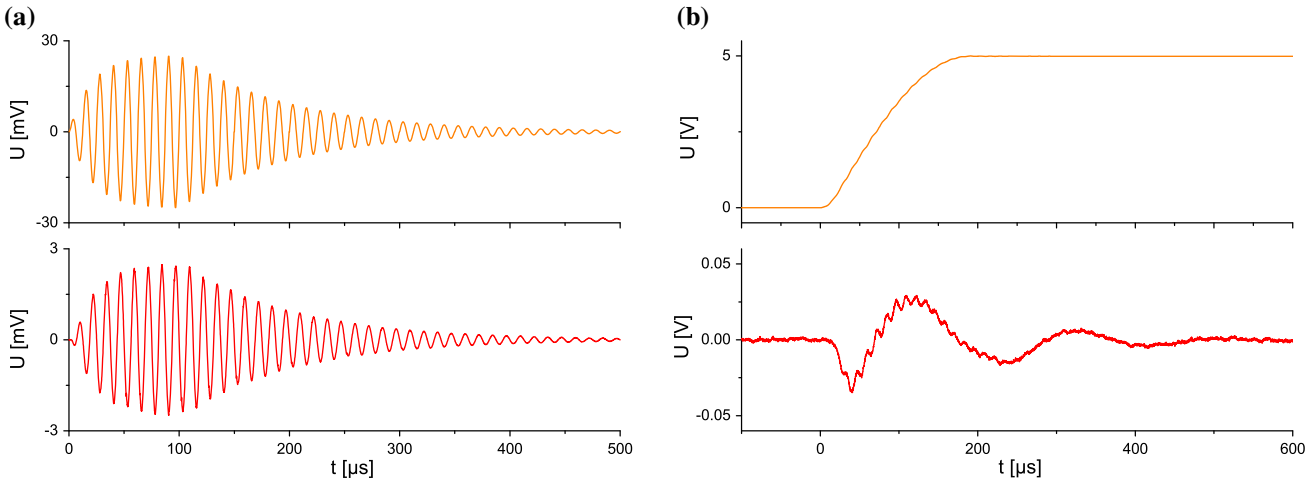

Fig. 8 **a** Oscillating part of the test function, generated by the arbitrary waveform generator (*top*) and measured with the sensor system (*bottom*). **b** Complete test function with base part and added oscillation (*top*) and the according measured signal (*bottom*)

varying fields could pass the bandpass filter (1 kHz high pass, 4th order Butterworth). Furthermore, the present acquisition electronics also have a frequency dependent transmission characteristic which influences the detected signal. The resulting signals resemble slow oscillations containing frequencies below 20 kHz. It turned out that the dominant part of this oscillation is the response of the sensor system to the first rise in the test signal. This rising is continuous and increasing over a time interval of approximately 20 μs. The signal is measured with a reversed polarity. The further behaviour of the test signal has no significant impact on the measured signal as long as the relaxation times are high enough. The measured signals are superimposed with a noticeable noise floor.

To test the response of the measurement chain to higher frequencies an oscillation with a frequency of 80 kHz was used (Fig. 8a, (top)). This oscillation is supposed to represent the signal that is generated by the vibration of the charged crack surfaces. Its rise and decay times would depend on the generation and relaxation of the charges and on the damping of the crack surface vibration. The envelope of this oscillation was chosen to increase within 100 μs and to subsequently decay to zero with a time constant of 100 μs. Figure 8a, (bottom) shows the response of the sensor system to the oscillation part only. For this part the rise and decay times and the frequency of the oscillation are measured unaltered. The polarities of the generated and the measured signals are reversed.

Combining base signal and oscillation part results in the test signal which is shown in Fig. 8b, (top). A ratio of 1/200 for the maximum amplitudes of the two parts was chosen. The measured voltage signal of the complete test signal is shown in Fig. 8b (bottom). The measured signal clearly shows the system response due to the rise in the base signal superimposed by the contributions of the 80 kHz oscillations. In summary the results of the experiments with the test source clearly indicate that the present measurement chain cannot detect frequencies below 1 kHz. Furthermore, if faster oscillations are superimposed with the slower field change they are detected almost unchanged.

2.2 Flexure Test Results

When the applied load exceeds ultimate strength complete cracking of the specimen occurs. The failure of each specimen results in one EME and AE signal to interpret. These signals are composed of many separate signals that are emitted during the crack propagation and are temporally and spatially close sources and thus merge into one EME and AE signal each. The crack dynamics are influenced by the stresses in different zones of the specimen. In bending tests there are generally two major zones, the tension zone and the compression zone. Therefore, the crack process consists of many separate steps with different characteristics. An image of the fracture surface after propagation of the cracks through the specimens is shown in Fig. 9. In this example the crack propagation starts at a point of high tension on the edge of the applied notch. Radial marks are visible which are parallel to the direction of crack propagation. Sliver like patterns indicate the region where crack branching took place and indicate an accelerating, unstable crack propagation. The upper half (compression zone) is mirror smooth with straight, horizontal rib marks (Wallner lines). This indicates smaller velocities and a propagation direction perpendicular to these lines. Since the crack surfaces are mostly smooth the crack area can be approximated by its height and width. The resulting crack surfaces are mostly parallel to the y-z-plane with a maximum deviation of 5°.

Figure 10 shows signals measured by the electromagnetic and the acoustic emission sensor for one representative

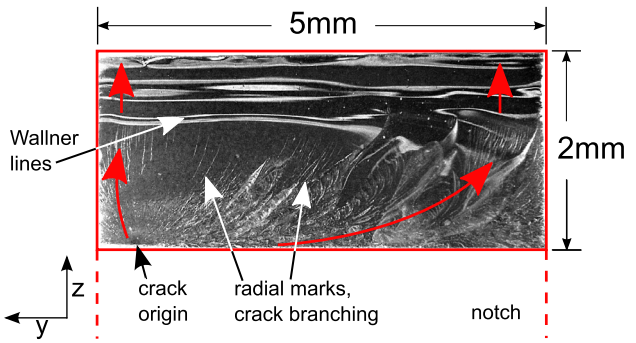

Fig. 9 Microscopy image of the crack area of a RTM6 specimen with parameters of the crack dimension. The *red arrows* indicate the crack propagation starting at a point on the applied notch. Two different areas of crack propagation are visible. A rough area with almost *radial marks* starting at the crack origin and a smooth area with *rib marks* at the upper half of the crack surface

specimen. The AE signal is influenced by the applied sensor as well as by the experimental setup. The acoustic emission sensor is attached to the fixture above the loading pin since the specimens are too small to directly attach the sensor on the specimen surface. Along the propagation path from crack to sensor the acoustic wave is influenced by damping and dispersion in the materials it propagates in and by reflection at the boundaries of the geometry.

According to the modelling results and our measurements with the test source the electromagnetic signals consist of several components which superimpose. The dominant part is a low frequency oscillation (as shown in Fig. 10a, top). This part relates to the charge separation during crack propagation. Based on our experiments with the test source this part is the system response of our measurement chain to the first 20 μs of a non-linear field rise. Oscillations with higher frequencies and smaller amplitudes are superimposed to the base signal. These signals are assumed to be caused by the vibration of the crack surfaces during and after crack initiation and propagation. In comparison to the base signal the ratio of amplitudes of these oscillations may appear much greater than they actually are. Figure 11a shows the frequency spectrum of the exemplary EME signal. For comparison, an exemplary noise measurement is displayed as well. The frequencies of the base part of the signal range from 1 kHz to approximately 20 kHz. Two other components are noticeable. A sharp peak at 41.2 kHz and a broader peak with a centre frequency of 76 kHz. The waveforms of these components were filtered using a 40–42 kHz and a 65–85 kHz bandpass filter and are displayed in Fig. 11b and c. Both resemble periodic oscillations with a distinct rise and decay. These components are supposed to originate from crack wall vibrations.

When comparing the EME signals and the AE signals (Fig. 10) one has to take into account that the AE frequencies are influenced by the geometry of the specimen and the propagation path from the source to the acoustic sensor [8,42]. Furthermore, only the propagation of the crack tip and the vibration of the crack surfaces contribute to the EME and the AE signal while the charge relaxation only contributes to the EME signal. When a 20–100 kHz bandpass filter is applied to the EME signals, most of the base part and the underlying noise is removed. The same filter applied to the AE signals partially removes spurious signals. However, the filtered EME and AE signals still differ in terms of frequency content, rise and decay time.

To characterize the present sensor system as well as the emitted field during crack initiation and propagation several flexure tests were performed. The distance d between the centre of the specimen and the EME sensor and the angle ϕ between the crack surface normal and the sensor plate normal were the varied parameters. To ensure statistical significance 6–8 specimens were tested for every point of measurement. The signals were individually analyzed by calculating the absolute energy using equation 7. Here $Z_M = 10\,k\Omega$ is the input impedance of the applied measurement equipment.

$$W = \frac{1}{Z_M} \int_{t_0}^{t_W} (U(t))^2 \, dt \tag{7}$$

The resulting energies were averaged to yield one data point. Although the specimens were prepared to be identical and were carefully placed and adjusted on the fixture, the EME and AE signals show a wide distribution in signal strength. This results in a high standard deviation of the calculated data, which is of the same order of magnitude for the EME and the AE signals. Thus, the cause for this high deviation is attributed to the complexity of the fracture process and not to the signal detection.

2.2.1 *Influence of Detection Angle*

While the sensor orientation was kept constant, the bend fixture was rotated orthonormal to the z direction. That way the angle between the crack surface normal and the sensor plate normal could be systematically changed. To investigate the influence of this angle on the EME signal strength the angle was varied between 0° (parallel) and 90° (perpendicular) in steps of 10°. The distance d of the sensor (see Fig. 4) was kept constant at 14 mm. For the recorded EME signals the absolute energies were quantified. Also, a band pass filter of 20–100 kHz was applied to the signals. Thus the base part and most of the underlying noise were removed leaving only the oscillating part of the waves. For the filtered signals the energies were quantified as well. The results are shown in Fig. 12.

A clear correlation between signal energy and detection angle is observable for both parts of the signals. While the

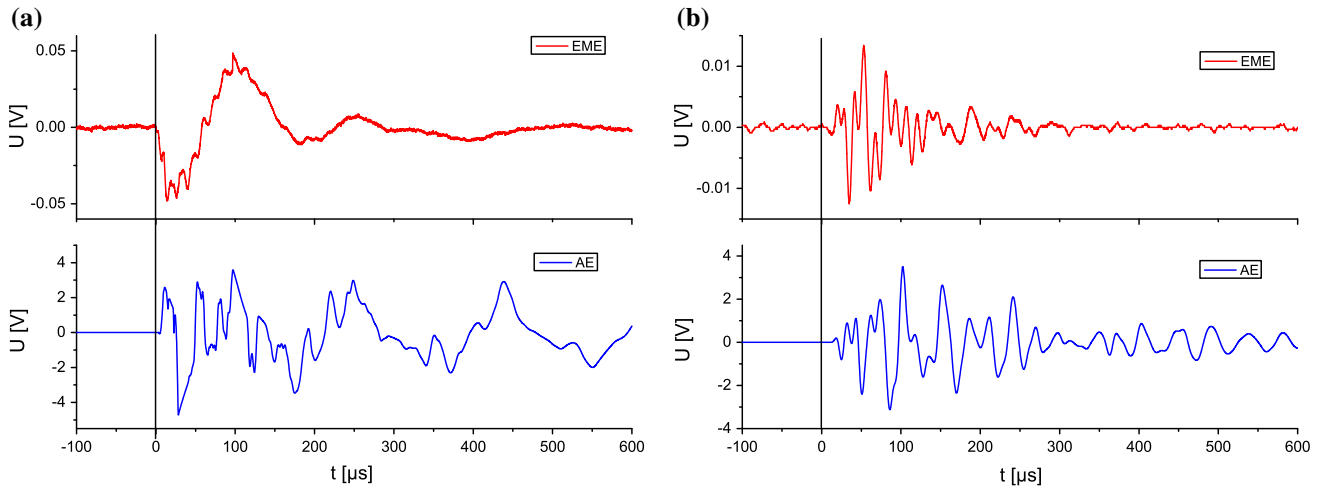

Fig. 10 **a** Typical pair of electromagnetic and acoustic signals obtained from the crack of one specimen. **b** Same signals with a 20–100 kHz bandpass filter applied

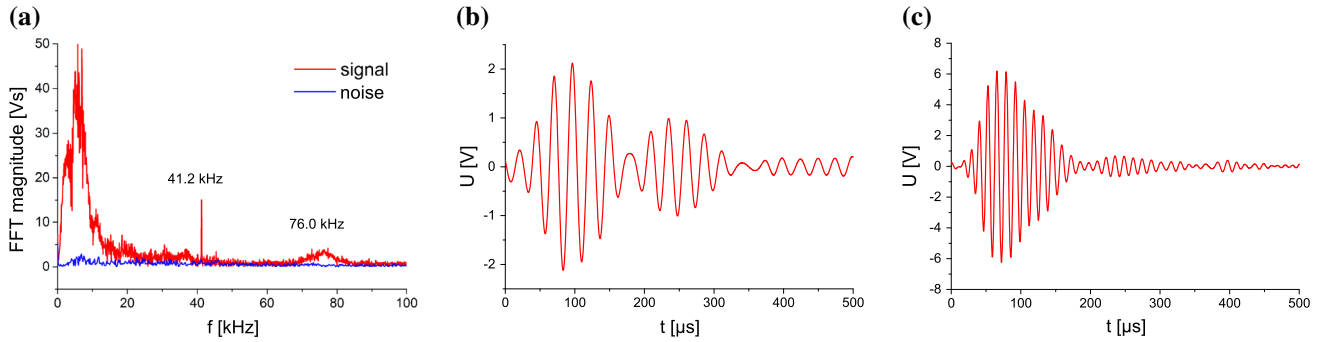

Fig. 11 **a** Frequency spectrum of the exemplary electromagnetic signal and, for comparison, an exemplary noise measurement (*blue*). **b** and **c** Temporal characteristics of the components labelled in the spectrum. **b** Signal with 40–42 kHz bandpass filter. **c** Signal with 65–85 kHz bandpass filter

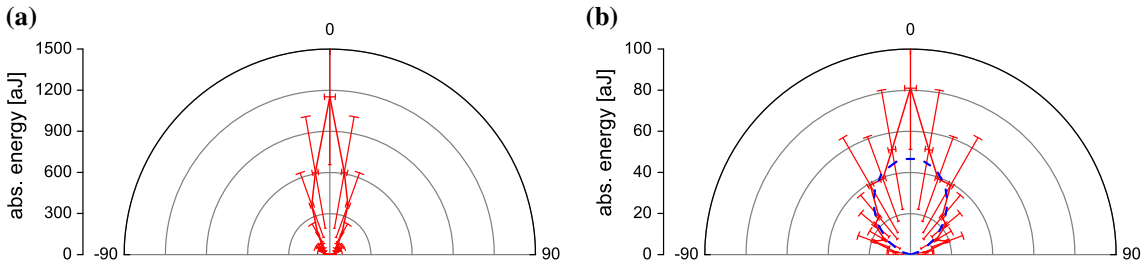

Fig. 12 Signal properties depending on detection angle. The data is mirrored at the 0° axis for clearness. **a** Angular dependence of the absolute energy of the whole signal. **b** Angular dependence of the absolute energy of the oscillating part of the signals and a scaled $\cos^2(\phi)$ graph (*dashed*)

strongest signals are detected for a parallel orientation of crack surface and sensor plate the measured signals decrease significantly in energy with increasing angle. This indicates a directional field distribution.

The angular directivity differs for the different parts of the signals. Figure 12 shows the calculated energies for the detected signals consisting of the base part and the oscillating part. The signals energy is dominated by the energy of the base part. The base signal is attributed to the separation of charges during crack growth. This part exhibits some kind of dipole characteristic, since two crack surfaces with opposite charges form a dipole moment with a direction parallel to the crack surface normal. The detected energies show a stronger angular dependence than the energies of the oscillating part. Only for angles up to 40° energies significantly exceeding the level of the noise were detected with a maximum at 0°. At $\phi = 10°$ the energy of the signals has dropped to 53 % when compared to the energy at $\phi = 0°$.

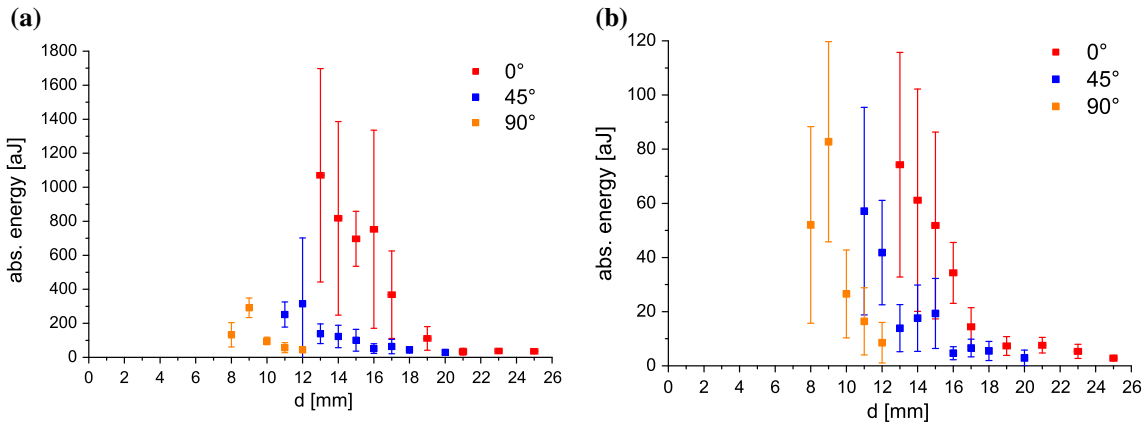

Fig. 13 **a** Dependence of the absolute energy of the whole signal on the source-sensor distance. **b**: Absolute energy of the oscillating part of the signals

The oscillating part of the signals is generated by the vibration of the crack surface. When this vibration is assumed to be perpendicular to the crack surface, i.e. has a strong directional orientation, an according angular dependence of the detected signals is expected. The behaviour measured seems to be more complex than one would expect for a simple dipole characteristic. For a point dipole the electric potential scales with $\cos(\phi)$, so one could expect the detected energy to scale with $\cos^2(\phi)$ (as indicated in Fig. 12b). The detected signal energies only partially fulfil this expectation. However, since the sensor is not point-like even for $\phi = 90°$ the sensor is likely to detect some field components of other angles. This could account for the stronger detection of energies for small angles then one would expect for a dipole characteristic.

Since the position of the AE sensor relative to the fixture and the specimen was not altered during these tests, the detected acoustic signals only scatter within the limits of their standard deviation. The signal strengths are evaluated with an averaged absolute energy of 614 ± 466 pJ.

2.2.2 *Influence of Sensor Distance*

One advantage of the dimensions of the specimens is the ability to position the EME sensor close to the crack for every orientation under observation. When the distance between the source of the electric field and a detector is increased a decrease in measured signal strength is assumed due to geometric spreading. Additionally the spatial characteristics of an electrical field depend on the type of source and on the surrounding matter. For example, the presence of conductors near a field source affects the field distribution. To measure the distance sensitivity of our sensor system we performed measurements of the EME signals for different distances between sensor and source. The signals were detected for three different angles ϕ. For angles of 0°, 45°and90° the distance of the sensing plate was varied ranging from the closest distance possible up to the distance where the signal-to-noise ratio inhibts detection of the signal. The recorded signals and the filtered signals (20–100 kHz bandpass filter) were then analyzed in terms of the detected energy. In Fig. 13 the results for the calculated energies are displayed for the whole signals (a) and for the oscillating part of the signals (b).

As expected, the measured energy decreases with increasing source-sensor distance. This was observed for all three angles. As discussed in the previous subsection the different parts of the signals show a different angular dependence. The dependence on the distance appears to be almost the same for the base signal and the oscillating part. For both parts the signals are only detectable within a distance of a few millimetres. The characteristics of the plotted data show no intuitive dependence of distance d. This may be due to multiple influences which all depend on the position of the sensor. The main effect is expected to arise from the spatial characteristic of the electric field. The potential generated by a dipole decreases with a $1/d^2$ dependence. This would result in a decrease with $1/d^4$ for the measured energies. Such dependence on distance was not observed. Since the real charge distribution is unclear, multipole moments of different order may also appear during the fracture process exhibiting different kinds of distance dependencies. Furthermore, with an increase of d the distance between the capacitor plates also increases and thus the capacitance decreases. For a constant field strength, the smaller the capacitance gets the higher is the resultant voltage between the plates. Another effect which might be of larger relevance than the increase of capacitance with distance is the influence of other conducting parts of the experimental setup. Although the fixture was build from non-conducting materials some other elements inevitably consist of conducting materials. The most important one is the AE sensor which is positioned 25 mm above the specimen. Since all conductors near the source influence the voltage on the

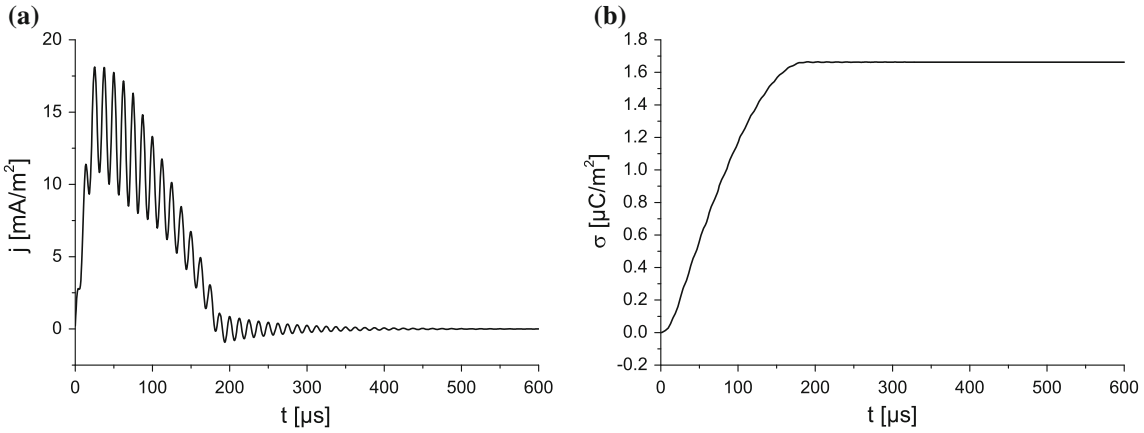

Fig. 14 **a** Time derivative of the surface charge density used as current source in the simulation. **b** Corresponding surface charge density consisting of a rising base signal and an oscillating part

sensor plate [34] this influence becomes more important at larger sensor distances.

The analysis of the according AE signals energies show no clear rising or decreasing trend and are considered constant within the limits of their standard deviation. For the angle of $\phi = 0°$ the absolute energy was averaged to 11.2 ± 1.8 nJ.

2.3 Modelling Results

In order to develop a EME source model, we incorporated the results from the tests with the artificial test source in the numerical simulations. For a time dependent charge distribution the potential at a fixed distance is proportional to the charge density. Thus, the temporal characteristic of the charge density used as model source was chosen to be proportional to the voltage which was generated by the arbitrary waveform generator for the test source experiments. Since the simulation model requires a current source as input the time derivative of the according experimentally applied test functions were used as the model source $Q_j(t) = \partial_t \rho(t)$. The utilized excitation function is shown in Fig. 14a. The corresponding surface charge density which resembles the test functions is shown in Fig. 14b and is composed of a rising part and an oscillation. The FEM model comprises the physics between the source and the sensor including the influences of the surrounding matter. The result of the simulation is the electric potential, averaged over the sensor surface, as a function of the source current (Fig. 15).

This calculated electric potential then is identical to the test signal (Fig. 8b, top). The calculated signal was then convolved with the systems transfer function to include the influence of the measurement chain. An input surface charge density with a maximum of 1.663 pC/mm^2 resulted in a simulated signal matching the amplitude of the experimental test source signals as seen in Fig. 16.

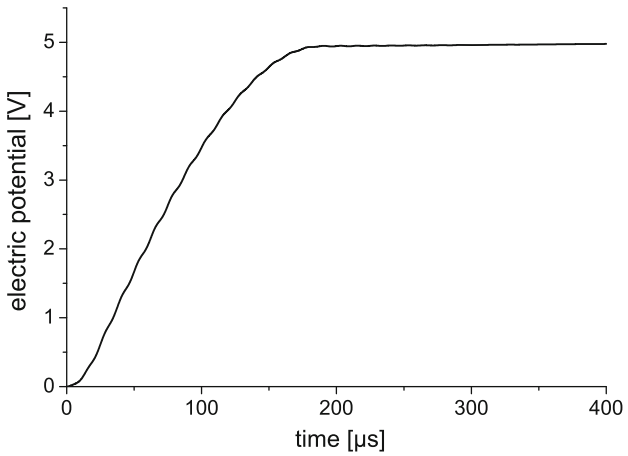

Fig. 15 Calculated electric potential at the sensor surface

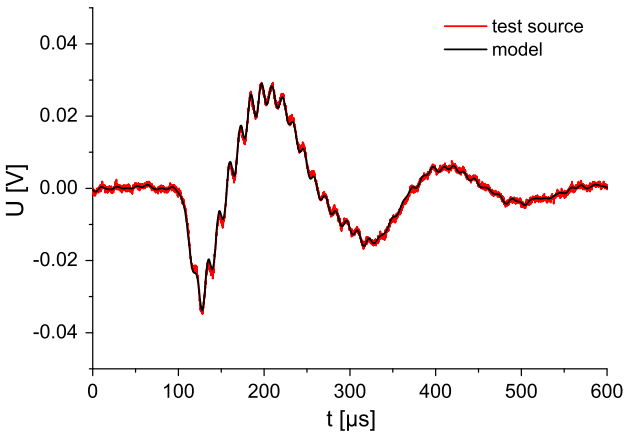

Fig. 16 Comparison of calculated and measured waveforms

This demonstrates that such charge distributions would result in EME signals that resemble the ones obtained during our fracture tests. Therefore, the proposed EME

source description is suitable to describe the experimentally obtained signals. In particular, we found that for a fixed source-sensor distance the potential at the position of the sensor is directly proportional to the electric charges present at the crack surface. The modelling results also point out the substantial influence of the applied measurement chain on the detected EME signal.

3 Conclusion

It was shown that the electromagnetic radiation emitted from fracture of a brittle dielectric consists of three different parts. A low frequency part originating from the rise of a charge imbalance during crack initiation and propagation. Its characteristics are determined by the temporal development of the position of the crack tip. The subsequent charge relaxation is a function of the dielectric properties of the material under investigation but is not being detected by the present acquisition system due to bandwidth limitations. This signal is superimposed with oscillations of higher frequencies and smaller amplitudes. The frequencies are approximately in the same range as the frequencies of the acoustic signals. These oscillations are considered to originate from the crack wall vibrations.

The signal strength of the recorded EME signals are highly dependent on the source-sensor distance and the orientation between sensor and crack surface. EME signals are only detectable within a range of a few millimetres and the strongest signals are measured with the sensor plate being parallel to the fracture surface.

A basic model of a time dependent surface charge density was developed that results in calculated signals that are in agreement with the experimentally detected EME signals. The temporal characteristic of the charge density simulates the accumulation of charges at the crack surfaces due to a propagating crack and an oscillation with a much smaller amplitude which reflects the vibration of the charged crack surfaces.

Important insights into the generation and the acquisition of EME signals from fracture were gained. Further experiments and an enhanced model which incorporates the actual crack dynamics are envisaged in the near future and are supposed to improve the understanding of the underlying physical phenomena.

The suitability of EME testing as a valuable NDT method has been indicated and we are currently focusing on the necessary steps to develop this technique to a nondestructive testing method.

Acknowledgments This research is funded by the DFG as part of the project "Relation of electromagnetic and acoustic emission to temporal and spatial crack motion on a microscopic scale in polymers and carbon fibers". We wish to thank Dr. S. Krohns, University of Augsburg, for the measurements of the dielectric properties of our specimens and for helpful discussions.

References

1. Yamada, I., Masuda, K., Mizutani, H.: Electromagnetic and acoustic emission associated with rock fracture. Phys. Earth Planet. Int. **57**, 157–68 (1989)
2. Frid, V., Rabinovitch, A., Bahat, D.: Fracture induced electromagnetic radiation. J. Phys. D **36**, 1620–1628 (2003)
3. Sedlak, P., Sikula, J., Lokajicek, T., Mori, Y.: Acoustic and electromagnetic emission as a tool for crack localization. Meas. Sci. Technol. **19**, 7 (2008)
4. Lacidogna, G., Carpinteri, A., Manuello, A., Durin, G., Schiavi, A., Niccolini, G., Agosto, A.: Acoustic and electromagnetic emissions as precursor phenomena in failure processes. Strain **47**, 144–152 (2010)
5. Misra, A., Prasad, R.C., Chauhan, V.S., Srilakshmi, B.: A theoretical model for the electromagnetic radiation emission during plastic deformation and crack propagation in metallic materials. Int. J. Fract. **2**, 99–121 (2007)
6. Sklarczyk, C., Winkler, S., Thielicke, B.: Die elektrische emission beim versagen von faserverbundwerkstoffen und ihren komponenten. Mat. Wiss. Werkstofftech. **27**, 559–566 (1996)
7. Koktavy, P., Pavelka, J., Sikula, J.: Characterization of acoustic and electromagnetic emission sources. Meas. Sci. Technol. **15**, 973–977 (2004)
8. Koktavy, P.: Experimental study of electromagnetic emission signals generated by crack generation in composite materials. Meas. Sci. Technol. **20**, 8 (2009)
9. Koshevaya, S., Grimalsky, V., Makarets, N., Kotsarenko, A., Siquieros-Alatorre, J., Perez-Enriquez, R., Juarez-Romero, D.: Electromagnetic emission from magnetite plate cracking under seismic processes. Adv. Geosci. **14**, 25–28 (2008)
10. Rabinovitch, A., Frid, V., Bahat, D.: Surface oscillations – A possible source of fracture induced electromagnetic radiation. Tectonophysics **431**, 15–21 (2007)
11. Miroshnichencko, M., Kuksenko, V.: Study of electromagnetic pulses in initiation of cracks in solid dielectrics. Sov. Phys. Solid State **22**, 1531–1533 (1980)
12. O'Keefe, S.G., Thiel, D.V.: A Mechanism for the production of electromagnetic radiation during the fracture of brittle materials. Phys. Earth Planet. Inter. **89**, 127–135 (1995)
13. Rabinovitch, A., Frid, V., Bahat, D., Goldbaum, J.: Fracture area calculation from electromagnetic radiation and its use in chalk failure analysis. Int. J. Rock Mech. Min. Sci. **37**, 1149–1154 (2000)
14. Laptukhov, A.I.: Generation of an electromagnetic field during rupture of a dielectric. Russian Phys. J. **38**, 15–19 (1995)
15. Baum, C., Breen, E., Giles, J., O'Nelll, J., Sower, G.: Sensors for electromagnetic pulse measurements both inside and away from nuclear source regions. IEEE antennas Propag. **26**, 22–35 (1978)
16. Tumanski, S.: Induction coil sensors – a review. Meas. Sci. Technol. **3**, R31–R46 (2007)
17. Kuechler, A., Dams, J., Dunz, T., Schwab, A.: Kapazitive sensoren zur messung transienter elektrischer felder und spannungen. Arch. Elektrotech. **68**, 335–344 (1985)

18. Partridge R E (1965) Capacitive probe E-field sensors. Sensor and simulation notes **11** 17pp.
19. Aydin, A., Stiffell, P.B., Prance, R.J., Prance, H.: A high sensitivity calibrated electric field meter based on the electric potential sensor. Meas. Sci. Technol. **21**, 5 (2010)
20. Winkler, S.: Tear detector for mechanical loading test sample–uses capacitive sensor coupled via impedance converter to electronic evaluation circuit patent DE **4004171**, C2 (1993)
21. Carpinteri, A., Lacidogna, G., Manuello, A., Niccolini, G., Schiavi, A., Agosto, A.: Mechanical and electromagnetic emissions related to stress-induced cracks. Exp. Tech. **3**, 53–64 (2012)
22. Chakravarty, A., Phillipson, T.E.: Triboluminescence and the potential of fracture surfaces. J. Phys. D **11**, 2175–2180 (2004)
23. Boltz, E.S., Fortunko, C.M., Hamstad, M.A., Renken, M.C.: Review of Progress in Quantitative Nondestructive Evaluation. Plenum Press, New York (1995)
24. Glaser, S.D., Weiss, G.G., Johnson, L.R.: Body waves recorded inside an elastic half-space by an embedded, wideband velocity sensor. J. Acoust. Soc. Am. **3**, 1404–1412 (1998)
25. Fish, J., Nath, A.: Adaptive and hierarchical modelling of fatigue crack propagation. Int. J. Numer. Meth. Eng. **16**, 2825–2836 (1993)
26. Hoppe, R.H.W., Petrova, S.I.: Multi-scale method for the crack problem in microstructural materials. Meth. Appl. Math. **1**, 19 (2010)
27. Sause, M.G.R., Horn, S.: Simulation of acoustic emission in planar carbon fiber reinforced plastic specimens. J. Nondestruct. Eval. **2**, 123–142 (2010)
28. Prosser, W.H., Hamstad, M.A., Gary, J., Gallagher, A.O.: Finite element and plate theory modeling of acoustic emission waveforms. J. Nondestruct. Eval. **3**, 83–90 (1999)
29. Sause, M.G.R., Hamstad, M.A., Horn, S.: Finite element modeling of lamb wave propagation in anisotropic hybrid materials. Compos. Part B **53**, 249–257 (2013)
30. Sause, M.G.R., Hamstad, M.A., Horn, S.: Finite element modeling of conical acoustic emission sensors and corresponding experiments. Sensor Actuat. A **184**, 64–71 (2012)
31. Coggon, J.H.: Electromagnetic and electrical modeling by the finite element method. Geophysics **1**, 132–155 (1971)
32. Jin, J.: The finite element method in electromagnetics. Wiley, New York (2002)
33. Moosburger-Will, J., Greisel, M., Sause, M.G.R., Horny, R., Horn, S.: Influence of partial cross-linking degree on basic physical properties of RTM6 epoxy resin. J. Appl. Polym. Sci **130**, 4338–4346 (2013)
34. Ramo, S.: Currents induced by electron motion. Proc. IRE **9**, 584–585 (1939)
35. Cooley, W.: Low-frequency shielding effectiveness of nonuniform enclosures. IEEE Trans. Electromagn. Compat. **1**, 34–43 (1968)
36. Lide, D.R.: CRC Handbook of Chemistry and Physics: A Ready-reference Book of Chemical and Physical Data. CRC Press, Boca Raton (2003)
37. Ranicar, J.H., Fleming, R.J., Legge, C.A.: Electrical conductivity in Poly(Vinyl chloride). Aust. J. Phys. **24**, 325–332 (1971)
38. Adamec, V., Mateová, E.: Electrical conductivity of PMMA at linearly increasing temperatures. Polymer **3**, 166–168 (1975)
39. Hector, L.G., Schultz, H.L.: The dielectric constant of air at radiofrequencies. Physics **4**, 133 (1936)
40. Pawar, S.D., Murugavel, P., Lal, D.M.: Effect of relative humidity and sea level pressure on electrical conductivity of air over Indian Ocean. J. Geophys. Res. **114**, 8 (2009)
41. Ivanov, V.V., Egorov, P.V., Kolpakova, L.A., Pimonov, A.G.: Crack dynamics and electromagnetic emission by loaded rock masses: translated from fiziko-tekhnicheskie problemy razrabotki poleznykh iskopaemykh. Sov. Min. Sci. **24**, 20–27 (1988)
42. Mori, Y., Obata, Y., Sikula, J.: Acoutic and electromagnetic emission from crack created in rock samples under deformation. J. Acoust. Emiss. **27**, 157–166 (2009)